Ultrawideband Underwater Acoustic Communication Channels

Paul A. van Walree, *Member, IEEE*, and Roald Otnes, *Member, IEEE*

Abstract—Traditional channel models for communications research are designed for narrowband systems. Underwater acoustic communication systems use a bandwidth that is not small compared with the center frequency of the signal and qualify as ultrawideband (UWB) in a relative sense. In this paper, measurements and analysis of acoustic propagation effects demonstrate the shortcomings of narrowband channel models. These effects are frequency-dependent fluctuation rates and frequency-dependent attenuation, where the frequency dependence of the attenuation differs between paths. This frequency selectivity of the medium violates the assumption of uncorrelated taps and requires a UWB channel model. It is also shown that correlative channel sounders preserve wideband properties, which renders them suitable for UWB channel simulation based on the principle of direct replay.

Index Terms—Fading statistics, path loss, underwater communications, wideband propagation channels.

I. INTRODUCTION

TRADITIONAL radio-frequency communication systems employ a bandwidth that is smaller than 1% of the center frequency of the signals. These systems are called narrowband, and have been the basis of a vast literature on channel models, modulation schemes, and channel simulators. During the past two decades, there has been a general trend in terrestrial wireless communications to increase the bandwidth occupied by the signals [1], [2]. The benefits include a proportional increase in data rate, robustness to fading, and possibilities for multiple channel access and covert communications. Systems whose bandwidth is between 1% and 20% of the center frequency are called wideband, and when the ratio exceeds 20% they become ultrawideband (UWB). There is also a UWB definition in terms of an absolute bandwidth of 500 MHz, regardless of the center frequency. The characteristics of the UWB propagation channel differ in a number of ways from classical narrowband channels [2].

Upon adopting the same definitions for the underwater acoustic domain, existing systems are at least wideband and many are UWB with a large relative bandwidth. The absolute bandwidth of acoustic communication systems is much smaller than that of their terrestrial counterparts, because of absorption in seawater [3], [4]. The attenuation increases with the frequency and with range. A popular frequency band for acoustic modems is 8–14 kHz (or about), with application ranges up to a few kilometers. Modem offerings are not limited to this band, however, and the research community is also known to explore different parts of the acoustic spectrum. For instance, Ochi *et al.* communicated over ranges of a few hundred meters in the 60–100-kHz band [5]. On the other end of the distance scale, Freitag and Stojanovic demonstrated the feasibility of basin-scale communications by demodulating acoustic tomography data [6]. Frequency band and range were 56–94 Hz and 3250 km, respectively. All these systems qualify as UWB in the relative sense.

There exists no typical acoustic channel [7]–[9], as different geographical sites, weather conditions, seasonal cycles, etc., have a large impact on the delay-Doppler spread, scattering and fading statistics, transmission loss, and ambient noise conditions. An acoustic communication system that works satisfactorily in one environment may fail to deliver in another one. More often than not, the UWB character of the channel is not explicitly taken into account in channel models used for transceiver algorithms and channel simulators. Wideband properties of acoustic communication channels are a largely unexplored area, and the objective of this paper is to reduce this knowledge gap with *in situ* measurements and analysis of channel parameters.

This paper is organized as follows. Section II presents an overview of popular channel models used by the research community, and discusses their completeness in terms of the propagation effects which they can represent. Section III provides a concise description of the sea experiments. Data analysis results are shown in Section IV, which demonstrates the occurrence of frequency-dependent fading statistics. In Section V, replay channel simulation reproduces the wideband effects of Section IV. Another replay example using a synthetic channel illustrates the differences between the narrowband and UWB channel models. Section VI summarizes the findings.

II. COMMUNICATION CHANNELS

The term channel model may denote a physical propagation model, but is also used for mathematical formulations of the channel impulse response. In both cases, a range of models exist with various levels of sophistication and completeness. Channel models are important in various branches of communications research, including channel simulation, modulation schemes, and

network simulations. In a linear time-variant channel, the output signal $y(t)$ follows from the input signal $x(t)$ via

$$y(t) = \int_{-\infty}^{\infty} h(t, \tau) x(t - \tau) \mathrm{d}\tau + n(t) \tag{1}$$

where $h(t, \tau)$ is the time-varying impulse response and $n(t)$ is additive noise. In the following, we use the term channel model for explicit expressions of $h(t, \tau)$.

A. Channel Models

A popular channel model in acoustic network simulations is the signal-to-noise ratio (SNR) model, e.g., [10] and [11]. Typically, a propagation model is used to compute the transmission loss of the modem signal, and empirical noise curves are used to obtain a noise level. The objective is to compute the relative strength of the signal and noise terms at the receiver. The equivalent channel model reads

$$h(\tau) = a\delta(\tau - \tau') \tag{2}$$

where τ' is the travel time and a is a constant related to the transmission loss. The travel time is important for network protocols, but irrelevant for the performance of the physical layer. Although the employed propagation model may implicitly or explicitly include multipath propagation, this information is only used to compute the transmission loss. The SNR channel model does not include signal distortion and assumes a noise-limited communication system.

Multipath propagation is addressed by the time-invariant narrowband (TINB) model, sometimes referred to as the Turin model [12]. It reads

$$h(\tau) = \sum_{n=1}^{N} a_n \delta(\tau - \tau_n) \tag{3}$$

where a_n is a complex weight with the magnitude and phase of the nth path arriving with a delay τ_n. A limitation of (3) is that it represents a static channel, while most acoustic channels are time variant, at least for a subset of the paths.

Time variability is readily included by allowing for amplitude and phase fluctuations via a time dependence of the weights a_n. This yields the time-varying narrowband (TVNB) channel model

$$h(t, \tau) = \sum_{n=1}^{N} a_n(t) \delta(\tau - \tau_n). \tag{4}$$

This model is widely used in the communications community, both for narrowband and wideband scenarios, and often successfully. However, it fails to address the frequency-dependent fading statistics which may characterize UWB propagation channels. An example is the signal power spectral density, which is affected by frequency-dependent loss mechanisms. In acoustic waveguides, there are multiple contributions to transmission loss. Loss due to geometrical spreading is independent of frequency, but absorption [3], [4], bottom loss [13], and surface loss [14] are frequency-dependent processes. The result is a skewed or otherwise distorted signal spectrum, which can be represented by the UWB channel model [15]

$$h(t, \tau) = \sum_{n=1}^{N} a_n(t) \chi_n(t, \tau) \otimes \delta(\tau - \tau_n) \tag{5}$$

where $\otimes$ denotes convolution and $\chi_n(t, \tau)$ gives the distortion of the nth path. If the input signal is white noise, the shape of the output signal spectrum at time t resulting from path n is the Fourier transform with respect to τ of $\chi_n(t, \tau)$.

UWB channel models using a constant $\chi_n(t, \tau) = \chi(\tau)$, independent of time and propagation path, have been used to deal with transceiver performance [16] and channel capacity [17] in the underwater domain. The measurements shown in Section IV-A of this paper reveal a channel characterized by $\chi_n(t, \tau) = \chi_n(\tau)$, with a frequency-dependent attenuation that differs between paths. The time dependence of $\chi_n(t, \tau)$ may not be needed for direct and bottom-reflected paths in a stationary deployment, but is required to account for the measurements in Section IV-B. In those measurements, all signal energy is received via scattering off a rough sea surface. Wind-generated waves are moving reflectors with time-varying roughness patterns. Moreover, breaking waves inject screens and plumes of air bubbles in the subsurface layer of the water column, which give rise to frequency-dependent absorption and scattering [18], [19]. Such a dynamic environment may be characterized by a time-varying frequency selectivity, represented via path distortion $\chi_n(t, \tau)$.

The UWB model has consequences for the statistical description of the channel. The concept of wide-sense stationary uncorrelated scattering (WSSUS) was developed for narrowband systems and uses correlated scattering to mean correlated taps in a tapped delay line [20]. In the channel of (5), the convolution smears out a single physical path over multiple taps. Neighboring taps are thus automatically correlated, even if the physical paths in the channel are uncorrelated.

Time-varying time delays in UWB channels can cause nonstationarity. The multiscale multilag (MSML) channel model [21], [22] addresses this phenomenon by treating the received waveform as a sum of signal copies with different lags and different Doppler scales. For tractability, it is often assumed that the delays are a linear function of time, i.e., that each path has a constant range rate $\alpha_n c$, where c is the sound speed. In that case, the MSML model follows from the UWB model by substitution of

$$\chi_n(t, \tau) = \mathrm{e}^{-i\alpha_n \omega_c t} \delta(\tau - \alpha_n t) \tag{6}$$

which yields

$$h(t, \tau) = \sum_{n=1}^{N} a_n(t) \mathrm{e}^{-i\alpha_n \omega_c t} \delta(\tau - \alpha_n t) \otimes \delta(\tau - \tau_n)$$
$$= \sum_{n=1}^{N} a_n(t) \delta(\tau - \tau_n - \alpha_n t) \mathrm{e}^{-i\alpha_n \omega_c t}. \tag{7}$$

The rotating phase factor $\exp(-i\alpha_n \omega_c t)$, where ω_c is the reference frequency of the complex baseband model (usually the

center frequency of the signal) is required to obtain the correct Doppler frequency shift. τ_n is the delay of path n at time $t = 0$. A wideband signal propagated through an MSML channel is subject to time compression/dilation, where the dilation factor differs between paths. The reason for extracting MSML as a special case of UWB is that MSML is the likely cause of the frequency-dependent fluctuation rates in Section IV-B. Note that the occurrence of time-varying delays has been demonstrated in various sea experiments, e.g., [9], [23], and [24]. These experiments also show that the assumption of constant range rates is not in agreement with all available measurements.

B. Response to Narrowband and Wideband Inputs

To be sure, narrowband channel models can be applied to wideband signals, and *vice versa*. It is instructive to examine the channel output (1), in the absence of noise, when the input signal is a sine wave

$$x(t) = e^{i\omega t}. \tag{8}$$

Since we work in the baseband domain, ω is the offset from the reference frequency ω_c of the complex baseband model. If we pass this narrowband signal through the TINB channel (3), we obtain

$$y(t) = e^{i\omega t} \sum_{n=1}^{N} a_n e^{-i\omega \tau_n}. \tag{9}$$

The output is a pure sine wave at the original frequency. Destructive interference may cause the multiplicative constant $\sum_{n=1}^{N} a_n e^{-i\omega \tau_n}$ to assume a small value at this frequency, which is known as signal fading. A wideband signal passed through the same channel suffers from frequency-selective fading.

A sine wave passed through the TVNB channel (4) becomes

$$y(t) = e^{i\omega t} \sum_{n=1}^{N} a_n(t) e^{-i\omega \tau_n}. \tag{10}$$

The intensity of the received narrowband signal is now time varying, and Doppler spreading occurs. The only contribution to Doppler spread is the time dependence of $a_n(t)$, so that the amount of frequency spreading does not depend on ω. In a wideband signal, the frequencies at which fading occurs have become time variant. Spectral nulls wander through the spectrum as the interference pattern varies. Complete signal fading is unlikely for large N and uncorrelated scattering.

A sine wave passed through the MSML channel (7) becomes

$$y(t) = e^{i\omega t} \sum_{n=1}^{N} a_n(t) e^{-i\omega \tau_n} e^{-i\alpha_n(\omega_c + \omega)t}. \tag{11}$$

Each path has a Doppler shift of $\Delta\omega = -\alpha_n(\omega_c + \omega)$, in addition to the Doppler spread due to the time variation in the weights $a_n(t)$. The fading rate due to time-varying constructive and destructive interferences between paths increases with ω,

since the phase term of each path rotates at a speed which is proportional to frequency. We can examine MSML signal fading in more detail by considering the received signal strength in a simple MSML channel with two paths

$$|y(t)|^2 = |a_1(t)|^2 + |a_2(t)|^2 + 2\Re\left[a_1(t)a_2^*(t)e^{-i\omega(\tau_1 - \tau_2)}e^{-i(\alpha_1 - \alpha_2)(\omega_c + \omega)t}\right] \tag{12}$$

where * denotes complex conjugate and $\Re$ is the real part. Using this expression as a starting point, a few special cases lend further insight. One special case is $a_1(t) = a_2(t) = a$, which yields a channel in which time-varying delays are the only cause of Doppler spreading

$$|y(t)|^2 = 2|a|^2 \left(1 + \cos\left[\omega(\tau_1 - \tau_2) + (\alpha_1 - \alpha_2)(\omega_c + \omega)t\right]\right). \tag{13}$$

The signal power is modulated by a sinusoid with an angular frequency $(\alpha_1 - \alpha_2)(\omega_c + \omega)$. A measure of the fluctuation or fading rate is the rate $R(\rho)$ at which the magnitude $|y(t)|$ of the complex envelope crosses a value ρ, either in the negative- or positive-going direction. $R(\rho)$ is known as the level crossing rate (LCR), formally defined in Section III-C and computed for acoustic data in Section IV-B. For the sinusoid in (13), the LCR is

$$R(\rho) = |\alpha_1 - \alpha_2|\frac{\omega_c + \omega}{2\pi}\left(\Theta(\rho) - \Theta\left(\rho - 2|a|\right)\right) \tag{14}$$

where Θ denotes the Heaviside step function. An important characteristic of (14) is that the fading rate is proportional to the passband frequency $\omega_c + \omega$. A necessary condition for this frequency dependence is that the channel is truly MSML, i.e., that there are at least two paths with different Doppler scales. If there is only one path $(a_2(t) = 0)$, (12) becomes

$$|y(t)|^2 = |a_1(t)|^2 \tag{15}$$

independent of frequency. If there are two paths, but with the same range rate $(\alpha_1 = \alpha_2)$, (12) reduces to

$$|y(t)|^2 = |a_1(t)|^2 + |a_2(t)|^2 + 2\Re\left[a_1(t)a_2^*(t)e^{-i\omega(\tau_1 - \tau_2)}\right] \tag{16}$$

where the only frequency dependence is a linear phase factor in the third term on the right-hand side. This expression includes the TVNB model $(\alpha_1 = \alpha_2 = 0)$ and yields a fluctuation rate which is governed by the time-varying weights $a_1(t)$ and $a_2(t)$, independent of the frequency.

These findings are also valid for channels with more paths, and are fundamental results. The contribution of $a_n(t)$ to the fading rate is independent of frequency, and the contribution of nonzero range rates is proportional to frequency. The linear frequency dependence also holds for time-varying range rates, as opposed to the constant range rates used in (7). In a channel whose time variability is dominated by the range rates, the Doppler spread increases linearly with the frequency, and the channel coherence time is inversely proportional to the frequency. Different sub-bands of a wideband signal have different coherence times in an MSML channel.

TABLE I
COMPLIANCE OF CHANNEL MODELS WITH PROPAGATION EFFECTS

	SNR	TINB	TVNB	MSML	UWB
Delay spread	No	Yes	Yes	Yes	Yes
Doppler spread	No	No	Yes	Yes	Yes
Freq. selective fading	No	Yes	Yes	Yes	Yes
Freq. dependent path loss	No	No	No	No	Yes
Freq. dependent fluct. rate	No	No	No	Yes	Yes
Dispersion	No	No	No	No	Yes

Finally, a sine wave passed through the UWB channel (5) becomes

$$y(t) = e^{i\omega t} \sum_{n=1}^{N} a_n(t) e^{-i\omega \tau_n} \xi_n(t, \omega) \qquad (17)$$

where $\xi_n(t, \omega)$ represents the time-varying frequency response of each path given by the Fourier transform

$$\xi_n(t, \omega) = \int_{-\infty}^{\infty} \chi_n(t, \tau) e^{-i\omega \tau} d\tau. \qquad (18)$$

Doppler spreading may occur due to the time dependence of $a_n(t)$ and the time dependence of $\xi_n(t, \omega)$. The latter includes the MSML mechanism, but another possibility is a time-varying distortion of paths at a fixed delay. The frequency dependence of $\xi_n(t, \omega)$ allows for a frequency-dependent path loss, an effect that none of the other models includes. A wideband signal passed through a UWB channel is shaped by all these effects.

It can be shown that the UWB model also allows for dispersion, which would cause the delay of each path to be a function of frequency. Dispersion in seawater is totally negligible at regular acoustic modem frequencies, but becomes noticeable with long-range signaling at very low frequencies; see, for instance, [25]. Dispersion has also been reported for propagation through sediments [26] and bubbly water [27].

Table I gives a summary of the capabilities of the presented channel models. The left column lists a selection of propagation effects that may affect the performance of communication systems. Noise is not considered here, but can be added to all model outputs using (1). Note that compliance in Table I does not imply that the correct mechanism is used. For example, Doppler spread in measured channels can be reproduced in simulation with TVNB, but if time-varying delays are the cause of the measured Doppler spread, the simulated channel will be fundamentally different from the ocean channel.

In communications, the term "path loss" is usually used similarly to the term "transmission loss" (or synonymously propagation loss) in underwater acoustics, in that they are measures of the *total* reduction in signal intensity between the sender and the receiver. For lack of a better term, Table I and the remainder of this paper use path loss in a broader sense, namely for the attenuation of *individual* propagation paths. The UWB model allows for attenuation whose frequency dependence is path dependent, and the measured delay profiles in Section IV-A are a striking example of such a channel. The possibility of a frequency-dependent transmission loss is included but not implied.

III. CHANNEL MEASUREMENTS

The data examined in Section IV were collected during two measurement campaigns. In both settings, an omnidirectional sender and an omnidirectional receiver were placed in stationary frames on top of sea mounts and ridges in a fjord environment. The analyses of the two experiments focus on frequency-dependent path loss and frequency-dependent fluctuation rates, respectively.

A. Experiment I

Experiment I used a setup with a transducer in the 4–8-kHz band and a distance of 3.9 km. The transmitter and receiver depths were about 75 m, and the maximum depth in-between was 200 m. Weather and wave conditions were calm. The channel is relatively static, with 90% of the signal energy being received via stable or slowly varying paths. From this experiment, a linear frequency-modulated (LFM) chirp probe signal is analyzed. The chirp sweeps from 4 to 8 kHz and has a length of 256 ms. Successive chirps are repeated head to tail during a total channel sounding duration of 16.9 s.

B. Experiment II

Experiment II used a setup with a transducer in the 10–20-kHz band and a range of 900 m. The transmitter depth was 26 m, the receiver depth was 21 m, and the maximum depth in-between was 70 m. The significant wave height was 0.4 m at the time of the measurement. An upward refracting autumn sound-speed profile trapped the sound in a surface duct, which ensured interactions with the waves. The contribution of stable paths is negligible, as virtually all signal energy is received via one or more surface bounces. Note that since the instruments are bottom mounted, all Doppler effects are due to variability of the propagation medium itself. In this case, the dynamic sea surface is the predominant cause of time variability.

The analysis of this experiment considers a multitone and a UWB probe signal. Fig. 1 depicts the received data by means of a spectrogram, which shows the spectral density of the data as it varies with time. The multitone probe is a sum of narrowband signals and consists of pure tones at frequencies of 10, 12, 14, 16, 18, and 20 kHz. The wideband probe is referred to as a pseudonoise (PN) probe. It consists of a maximum-length sequence with length $M = 255$, which is repeated 1026 times. Successive sequences are transmitted head to tail, which is required to obtain the well-known m-sequence autocorrelation function. A root-raised-cosine pulse shape is used with the rolloff factor 1/8. At a rate of $R_b = 8000$ b/s, the frequency band of the PN probe is flat from 10.5 to 17.5 kHz, has -3 dB points at 10 and 18 kHz, and falls off rapidly beyond this range. Both probe signals have a length of $T \approx 32.7$ s.

C. Data Processing

The recorded LFM and PN probes are used to obtain an estimate of the channel impulse response. They are processed in a routine fashion by correlation with the transmit chirp (m-sequence) and stacking successive channel snapshots [9], resulting in a bandlimited channel estimate $\hat{h}(t, \tau)$. On the other hand, the sum of sine waves is processed for narrowband
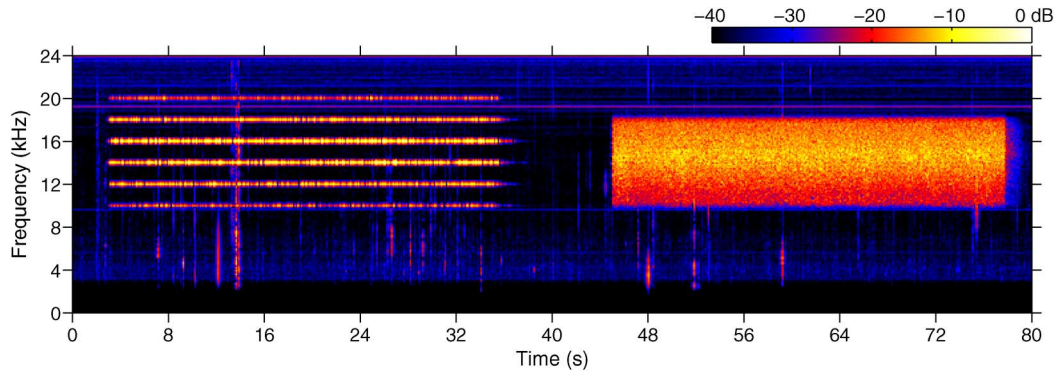
Fig. 1.   Spectrogram of recorded data: multitone waveform and pseudonoise probe (experiment II).

fading statistics. The received data are basebanded for each tonal frequency, and the Doppler power spectrum

$$S(\Delta\omega) = \mathbb{E}\left\{ \frac{1}{T} \left| \int_0^T y(t)\exp(-i\Delta\omega t)dt \right|^2 \right\} \qquad (19)$$

is extracted. For the remaining computations, the baseband signal is first passed through a bandpass filter with a width of 50 Hz. Subsequently, it is root mean square (RMS) normalized to yield the dimensionless magnitude

$$\tilde{y}(t) = |y(t)| \left(\frac{1}{T} \int_0^T |y(t)|^2 \, dt \right)^{-1/2}. \qquad (20)$$

Quantities extracted from $\tilde{y}(t)$ are the probability density function (PDF)

$$D(\rho) = \frac{P[\tilde{y} \geq \rho, \tilde{y} < \rho + \Delta]}{\Delta} \qquad (21)$$

and the level crossing rate (LCR)

$$R(\rho) = \frac{P[\tilde{y}(t + \Delta t) \geq \rho, \tilde{y}(t) < \rho]}{\Delta t}. \qquad (22)$$

The LCR is a measure of the fluctuation rate of a signal and tells how often the magnitude of the complex envelope crosses level ρ in the positive-going direction. It was already introduced in (14) in the discussion of MSML fading characteristics.

IV.   RESULTS AND DISCUSSION

A. Experiment I: Frequency-Dependent Path Loss

Fig. 2 shows the channel estimate $\hat{h}(t,\tau)$ obtained with the chirp train of Experiment I. The exact travel time between the sender and the receiver is not known, and the strongest arrival is arbitrarily placed at zero delay. The main paths arriving between -20 and 20 ms are relatively stable, whereas the delayed cluster of arrivals between 50 and 60 ms exhibits time variability.

The power delay profile $\hat{P}(\tau) = \int |\hat{h}(t,\tau)|^2 dt$ characterizes the distribution of received signal power over delay. It is possible to estimate the delay profile in different sub-bands of the 4–8-kHz band by limiting the sounder to sub-bands. This can be
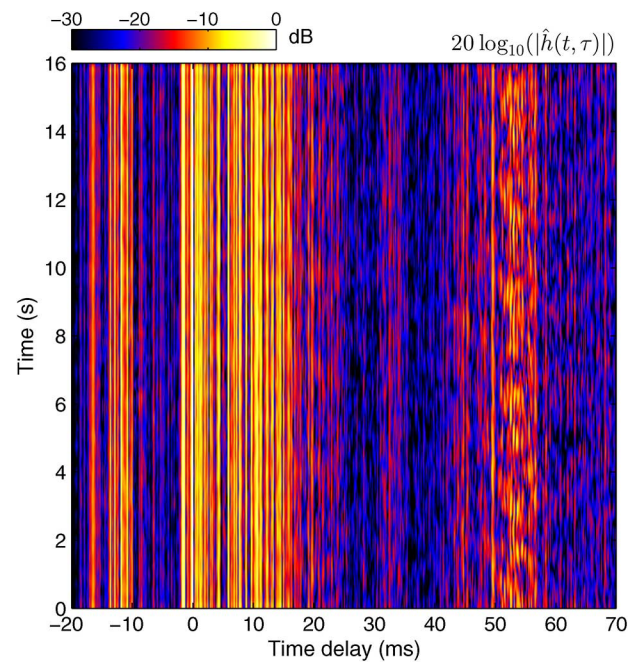

Fig. 2.   Experiment 1: Magnitude of $\hat{h}(t,\tau)$ obtained with the chirp sounder.

done by applying a bandpass filter to the received signal and/or the chirp replica. Any contiguous sub-band of an LFM is another LFM, with LFM autocorrelation properties, but, of course, there is a tradeoff between bandwidth and resolution in delay.

Fig. 3 shows power delay profile estimates for the same data shown in Fig. 2, but in three frequency bands. The profiles for the 4–5- and 7–8-kHz sub-bands are strikingly different, as it is not even apparent that they represent the same channel. The 4–8-kHz profile features a higher resolution in delay because of the larger measurement bandwidth, and is an average over the overall band.

To examine in more detail how the profile varies with frequency, it is computed in multiple overlapping sub-bands. These bands have a width of 800 Hz, a spacing of 50 Hz, and Hamming tapering on the part of the replica corresponding to each sub-band. The result is presented in Fig. 4 and shows that there is significant variation of path loss over the band. Recall that this paper considers the term "path loss" in relation to individual paths. The relative path strengths in Figs. 3 and 4 vary strongly
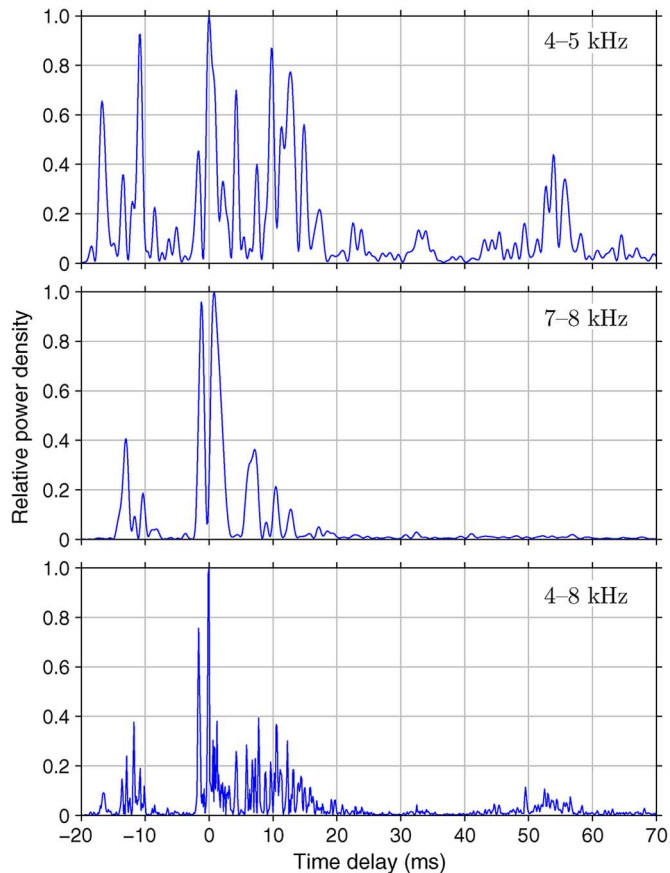
Fig. 3. Experiment I: Power delay profiles of a single acoustic transmission, averaged over 17 s, computed for three frequency bands. The profiles are individually normalized to a peak value of 1.
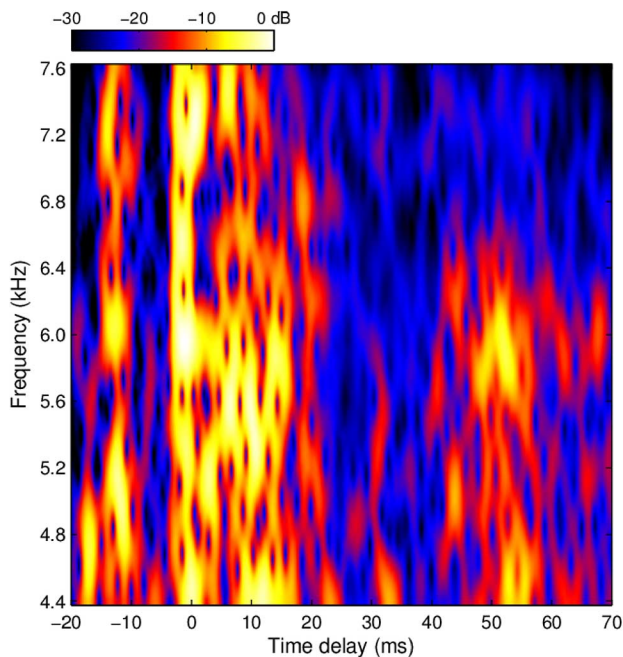

Fig. 4. Experiment I: Estimate of the power delay profile as a function of frequency. The profiles for sub-bands are not individually normalized.

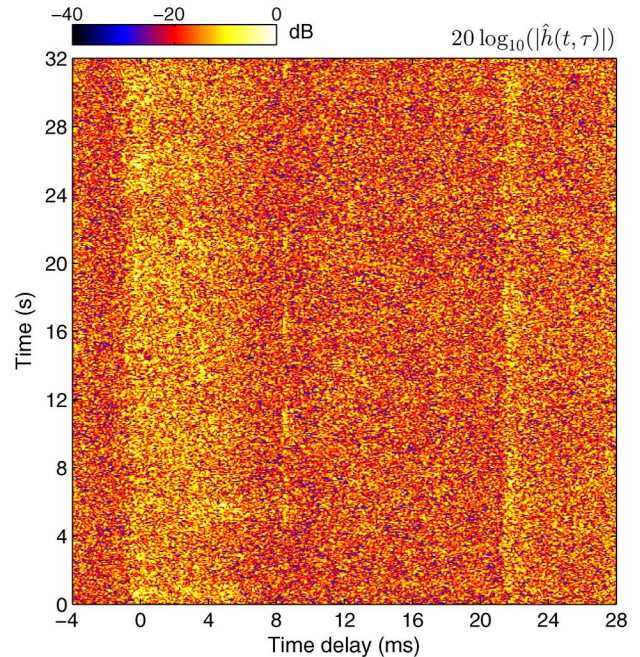with the frequency. Presumably there is also a frequency dependence of the transmission loss, but measurement of this quantity would require a calibrated measurement chain.

Fig. 5. Experiment II: Magnitude of $\hat{h}(t, \tau)$ obtained with the PN probe signal.

From the models discussed in Section II, only UWB can account for the observed frequency dependence. For TVNB and MSML, the relative path strengths are $\mathbb{E}\{|a_n(t)|^2\}$, independent of frequency, while UWB has $\chi_n(t, \tau)$ to tailor the frequency selectivity of each path. By saying this we assume that a path is a single path, and not a collection of unresolved micropaths. Unresolved paths may give rise to frequency-selective destructive and constructive interference, in the same manner as (4), even if the micropaths themselves do not have a frequency-dependent attenuation. This can explain the waviness observed in Fig. 4, but not the disappearance of energy in a large part of the frequency band (e.g., between 50 and 60 ms above 6.4 kHz).

B. Experiment II: Frequency-Dependent Fluctuation Rates

Fig. 5 shows the magnitude of $\hat{h}(t, \tau)$ for the PN probe shown in Fig. 1. In this experiment, the rough sea surface acts as a continuum of moving scatterers. The resulting channel has a densely populated, rapidly varying impulse response and looks like clutter everywhere, without individually identifiable paths such as in Fig. 2. Note that channel estimates obtained with a correlative sounder are susceptible to systematic measurement errors [28]. In the present case, the errors are nonnegligible as the channel under examination is overspread. To capture the channel fluctuations we have chosen to analyze a wideband probe signal with a short tracking period. An unavoidable consequence is aliasing in delay, which is the dominant measurement error in Fig. 5. The true channel has an impulse response which is longer than the 32-ms tracking period of the PN probe. Arrivals with a delay exceeding 32 ms are aliased and end up at false taps in Fig. 5.

The only factor which degrades the fidelity of the measured narrowband fading statistics is noise, but its effect is small since the SNR of the recorded data is high. Fig. 6 shows the PDF for
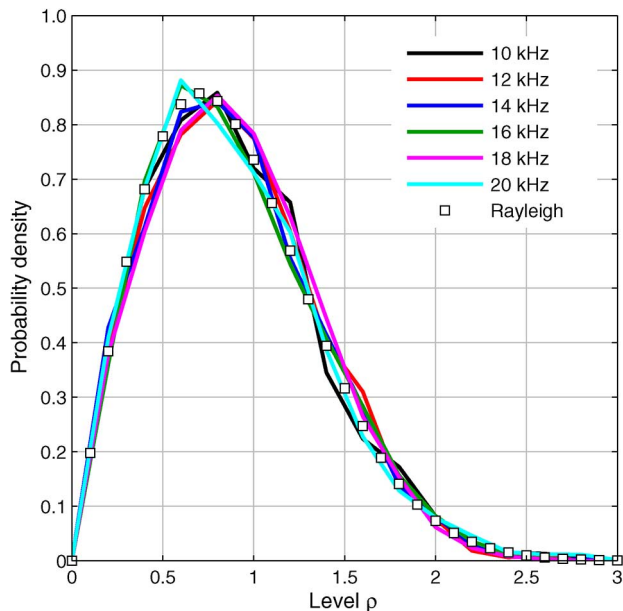
Fig. 6. Experiment II: Narrowband probability density functions for *in situ* measurements.

Fig. 8. Experiment II: Normalized power spectral densities for *in situ* measurements.
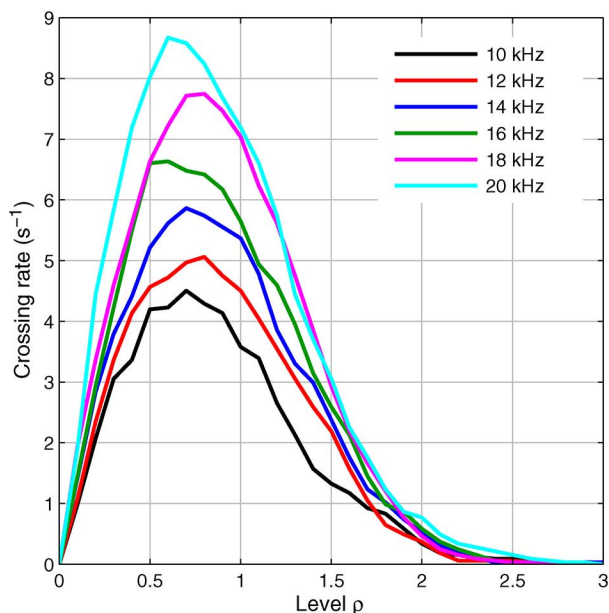

Fig. 7. Experiment II: Narrowband level crossing rates for *in situ* measurements.

the received narrowband signals. The PDFs are independent of frequency and well described by the Rayleigh distribution

$$D_{\mathrm{R}}(\rho) = \frac{\rho}{\sigma^2} \exp\left(-\frac{\rho^2}{2\sigma^2}\right) \tag{23}$$

which is included in the figure for $\sigma = 1/\sqrt{2}$. There is no frequency selectivity in the PDF.

The wideband character of the channel becomes apparent from the level crossing rates in Fig. 7. These curves also have a Rayleigh shape, consistent with a Rayleigh fading channel [29], but with a frequency-selective scaling factor. Within the uncertainty of the measurement, the fluctuation rate increases linearly with frequency. A higher fluctuation rate suggests a broader
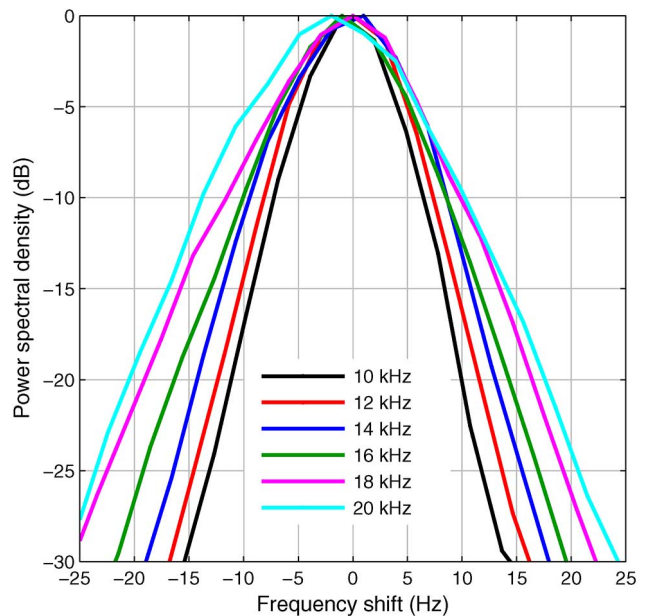
Doppler spectrum and shorter coherence time. This is confirmed by the Doppler power spectra in Fig. 8, whose width increases with the frequency.

The UWB model has two mechanisms at its disposal to account for frequency-dependent fluctuation rates. One mechanism is the MSML way with time-varying delays. The linear frequency dependence of the LCR agrees with MSML, as explained in Section II-B, and suggests that MSML is the dominant cause of Doppler spreading in this channel. Wandering delays in an MSML channel are often readily noticed by visual inspection of $\hat{h}(t,\tau)$, e.g., [9], [23], and [24]. In Fig. 5, this is not the case, but the effect might be present on a microscopic scale, or be obscured by the high density of arrivals, the fluctuating weights $a_n(t)$, or the aliasing. However, in the absence of MSML propagation, the UWB model can account for frequency-dependent fluctuation rates by other means. This will be illustrated in Section V.

V. CHANNEL REPLAY AND SIMULATION

A. Replay of Ocean Channels

The question may be asked to what extent a correlative sounder preserves the wideband character of a channel. Do the channel soundings $\hat{h}(t,\tau)$ preserve the frequency-selective fading statistics of the ocean channels? To answer that question we pass the LFM and multitone probes through replay channels. Replay is a channel simulation technique that uses a channel estimate obtained by measurement to filter input waveforms. Distinction is made between direct replay and stochastic replay [30], [31]. Direct replay uses the measured $\hat{h}(t,\tau)$ directly, whereas stochastic replay attempts to synthesize a channel whose statistical properties are in agreement with those of $\hat{h}(t,\tau)$. In the following, we use direct replay:

$$y(t) = \int_{\tau_1}^{\tau_2} \hat{h}(t,\tau) x(t-\tau) \mathrm{d}\tau \tag{24}$$
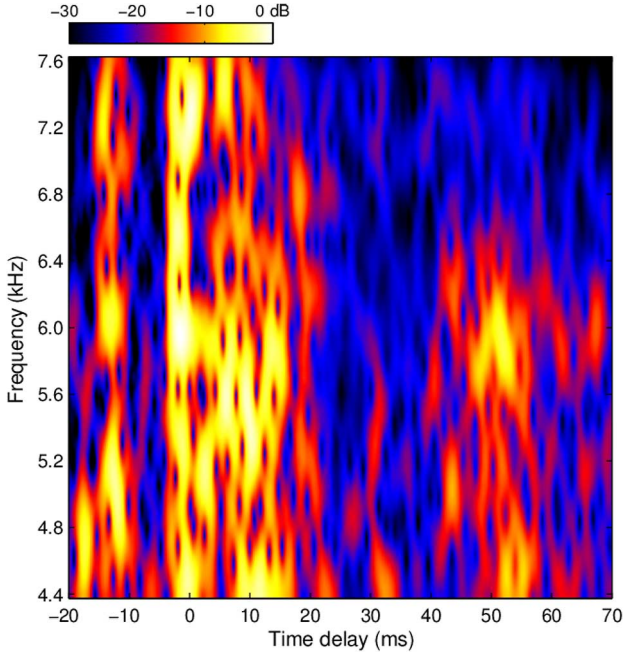
Fig. 9. Delay profile versus frequency, using direct replay of the channel of Section IV-A (experiment I).
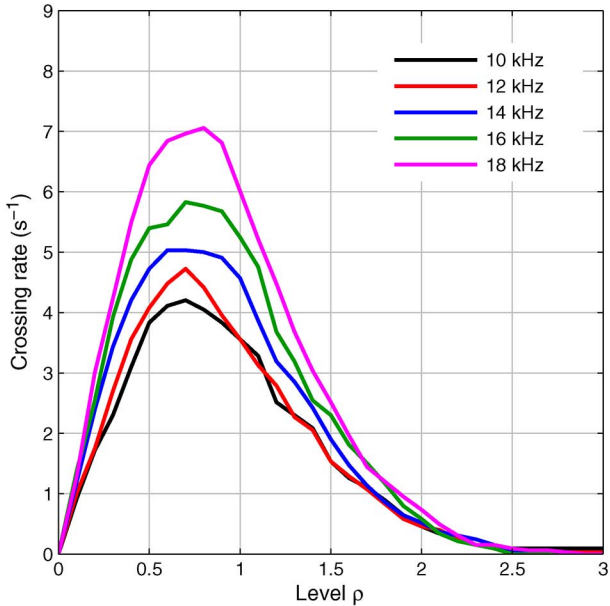

Fig. 10. Narrowband level crossing rates, using direct replay of the channel in Section IV-B (experiment II).

where $\tau_2 - \tau_1$ is the delay coverage of the probe signal, which equals the pulse repetition time. In the discrete-time implementation of (24), we use linear interpolation to upsample $\hat{h}(t, \tau)$ from the channel tracking rate $(\tau_2 - \tau_1)^{-1}$ to the sampling frequency of the input signal $x(t)$. For experiment I, the input signal is the same LFM probe that was used to obtain $\hat{h}(t, \tau)$. For experiment II, the input signal is the multitone probe, whereas $\hat{h}(t, \tau)$ was obtained with the PN probe. The output of the channel replay is analyzed in the same manner as the acoustic data.

The answer to the above question is affirmative. Fig. 9 demonstrates that the frequency-dependent path loss is captured by the sounding. The graph is almost indistinguishable

from the original measurement in Fig. 4. Furthermore, Fig. 10 reproduces the frequency dependence of the LCR. The curves are a bit lower than in Fig. 7, which is due to the loss of signal power at large frequency shifts. The replay channel is limited to the Doppler regime between -15.7 and $+15.7$ Hz, which according to Fig. 8 misses a small part of the signal power. This power is aliased in the Doppler spectrum of the sounding. Moreover, the frequency response of the linear interpolation is not flat and reduces the power spectral density toward the Nyquist frequency of the sounder. Despite the slightly lower LCRs in the replay channel, the qualitative agreement between Figs. 10 and 7 is convincing.

The 20-kHz signal is omitted from Fig. 10, because the PN probe has no coverage at this frequency. Furthermore, the 14-kHz tone is actually played at 14.1 kHz in the replay channel. The reason is that the PN baseband signal has zero mean, which becomes a spectral null at its center frequency in passband. Replay at 14 or 20 kHz produces nonsense, because a response that has not been measured cannot be reproduced.

B. Replay of a Synthetic Channel

As explained in Section II-B, MSML propagation yields fading rates which increase with the frequency. The UWB model can produce frequency-dependent fluctuation rates with two mechanisms. It can use the MSML way with time-varying time delays, or it can apply a time-varying frequency selectivity to paths at a fixed delay. A fundamental difference is that the latter mechanism can achieve the objective with a single path, while the MSML mechanism requires at least two paths with different Doppler scales. In the simulation that follows, we will illustrate how the UWB model can represent frequency-dependent fading rates with a single path at a fixed delay. Simultaneously, the simulation serves to illustrate the fundamental difference between narrowband and UWB channel models.

The PN probe signal $x(t)$ is split into two sub-bands by passing it, in parallel branches, through a lowpass filter and a highpass filter cutting at 14 kHz. This yields $x_\ell(t)$ and $x_h(t)$, respectively. Two random white noise signals are passed through lowpass filters operating between 0–0.2 and 0–1 Hz, which yield $w_\ell(t)$ and $w_h(t)$, respectively. Three synthetic channels are subsequently constructed via

$$[ch1] \quad y(t) = x(t) \tag{25}$$

$$[ch2] \quad y(t) = [w_\ell(t) + w_h(t)] \, x(t) \tag{26}$$

$$[ch3] \quad y(t) = w_\ell(t) x_\ell(t) + w_h(t) x_h(t). \tag{27}$$

Channel 1 is ideal, channel 2 is narrowband and flat fading, and channel 3 has wideband properties. Channel 3 is unrealistic, but illustrates the wideband principles well. Its effect is seen in Fig. 11(a). Two sub-bands have been established with different fading rates.

The probes passed through the simulated channels are fed to the correlation estimator, which outputs the channel estimates $\hat{h}_k(t, \tau)$, $k = 1, 2, 3$. The three cases are compared in Fig. 12, which plots $\hat{h}_k(t, \tau)$, and Fig. 13, which gives the corresponding delay profiles $\hat{P}_k(\tau)$. The figures zoom in on the only path. Systematic measurement errors are absent for channel 1, except for
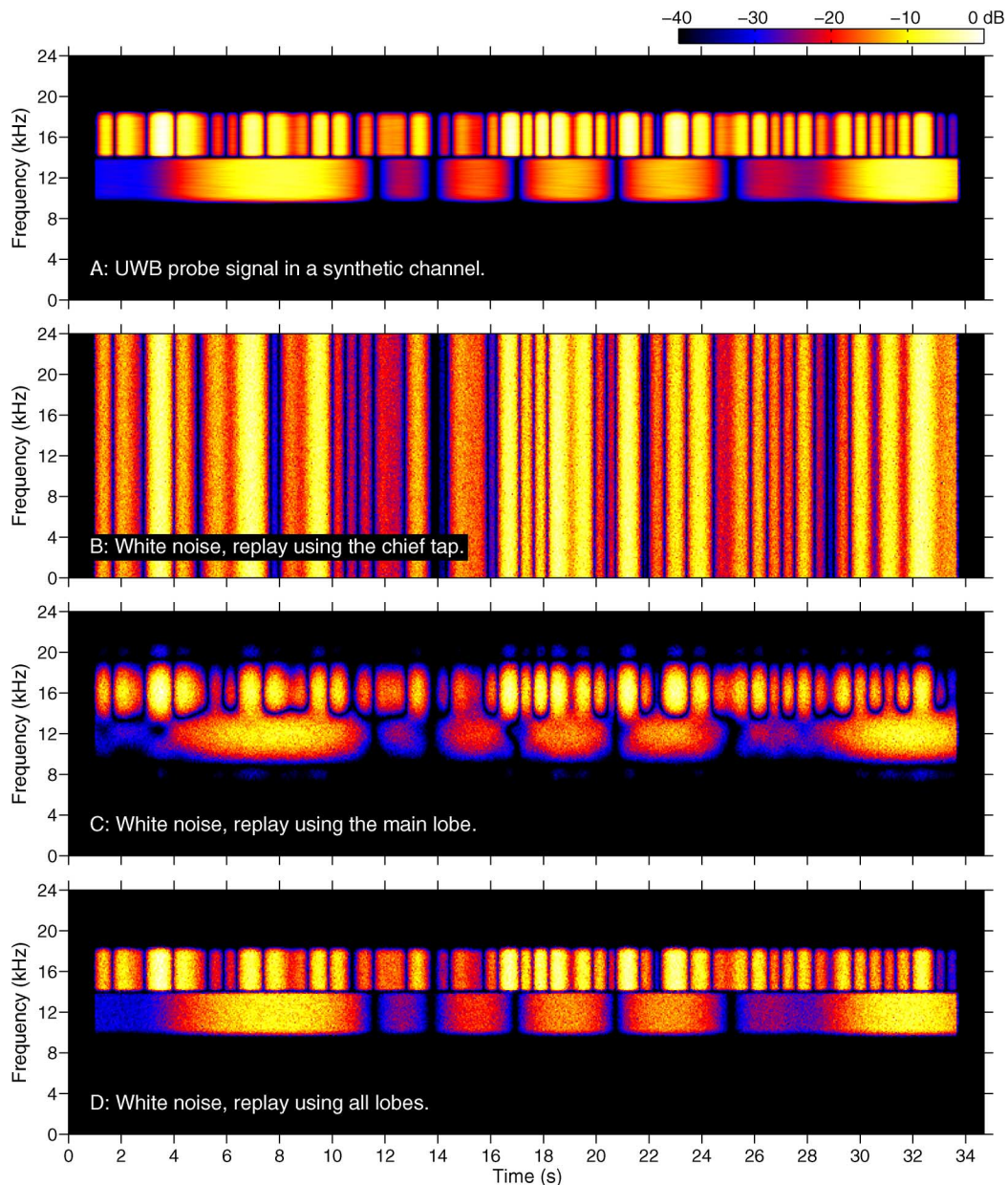
Fig. 11.   Signal spectrograms. (a) The PN probe distorted by the channel represented by (27). The other panels are for white noise passed through the $\hat{h}_3(t, \tau)$ replay channel using (b) the chief tap, (c) the main lobe, and (d) all lobes.

the pulse-compression error [28]. This error arises because the autocorrelation function of the m-sequence is not a delta function, but has a relative sidelobe level of $-20 \log_{10}(M) = -48$ dB. The channel estimate shows power at delays where the true channel has no power. There are also stronger sinc-like sidelobes due to the spectrum of the probe signal, whose shape approaches a rectangle. These sidelobes and the finite width of the main lobe are not measurement errors, but reflect a bandlimited sounding.

In Fig. 12, $\hat{h}_2(t, \tau)$ equals the product of $\hat{h}_1(t, \tau)$ and $a_1(t) = w_l(t) + w_h(t)$. The time-varying weight simply modulates the amplitude of the path. This is not the case for $\hat{h}_3(t, \tau)$, which looks different. The main lobe of the path broadens, structures appear, and the overall sidelobe level increases. This is more clearly visible in Fig. 13. $\hat{P}_2(\tau)$ is the same as $\hat{P}_1(\tau)$, which illustrates that time variability alone does not deform the profile.

$(\hat{P}_2(\tau)$ would differ from $\hat{P}_1(\tau)$ in rapidly varying channels, when channel fluctuations within a sounding pulse affect its autocorrelation function.)

Channel 3 is well suited to illustrate the difference between narrowband and UWB channel models and the effect of path distortion. To this end, $\hat{h}_3(t, \tau)$ is used for a replay experiment with white noise as the input signal. Using only the dominant tap ($\tau = 0$) in the replay, the output exhibits flat fading over the entire band of the input signal: Fig. 11(b). This is a discrete-time implementation of the TVNB model with one path. The outcome is the same as that of a replay channel using the chief tap of $\hat{h}_2(t, \tau)$, which says that the center tap of $\hat{h}_3(t, \tau)$ represents $w_l(t) + w_h(t)$, i.e., the sum of the sub-band modulations. Use of the main lobe of $\hat{h}_3(t, \tau)$ ($|\tau| \leq 0.25$ ms) has a bandlimiting effect and roughly reproduces the spectrogram of the probe signal. Use of all sidelobes ($|\tau| \leq 3$ ms) in the replay
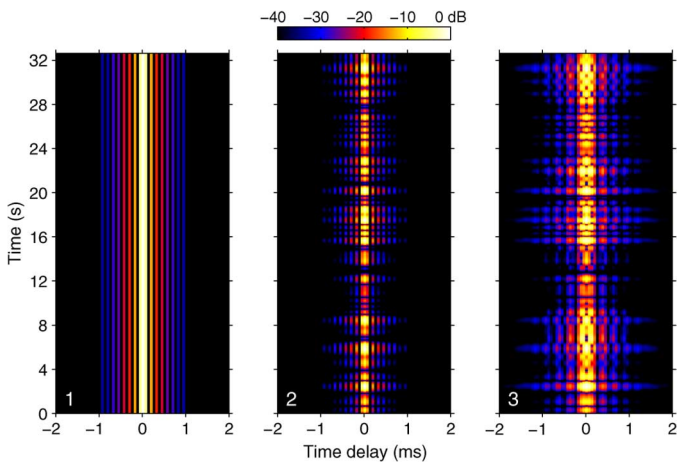
Fig. 12. Magnitude of $\hat{h}_k(t, \tau)$ in three monopath channels. $k = 1$: ideal channel; $k = 2$: flat fading; $k = 3$: frequency-selective fading.
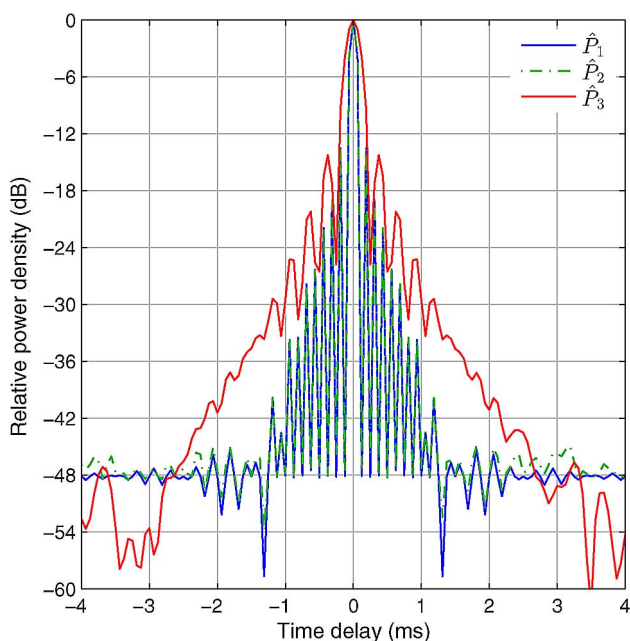

Fig. 13. Normalized delay profiles for $\hat{h}_1$, $\hat{h}_2$, and $\hat{h}_3$.

results in Fig. 11(d) with perfect reconstruction of the original spectrogram. This last replay experiment represents the UWB model in full and illustrates that this model can account for frequency-selective fluctuation rates, even for a single path at a fixed delay. The sidelobes in delay, which represent $\chi_n(t, \tau)$, are of crucial importance for the completeness of the channel description.

C. Discussion

It is not known whether time-varying path distortion contributes to our measurements, but we cannot rule out that it plays a role. Physically, it would correspond to the sea surface acting as a mirror with a time-varying frequency dependence of its reflection coefficient, for instance, because of changes in the population density of subsurface air bubbles. Nonetheless, the

main candidate to explain Fig. 7 remains MSML. It correctly predicts the linear frequency dependence, and various measurements have demonstrated the presence of MSML in sound reflected by a wavy sea surface [9], [23], [24], [32]. Unfortunately, the channel sounding in Fig. 5 is so crowded that individual paths or time-varying delays are not recognized in our case. However, MSML propagation is expected in the surface duct of experiment II. Rays reflected by different parts of the sea surface experience reflectors with different velocities, and at any point in time there will be a spread of range rates in the reflected sound. At a given frequency, this gives rise to a Doppler spread in the received signal. Since the Doppler shift brought about by a moving reflector is proportional to the frequency, the Doppler spread increases with frequency, as in Fig. 8.

VI. CONCLUSION

Frequency-dependent path loss and frequency-dependent signal fluctuation rates have been measured. The importance of these effects for acoustic communication systems and research depends on their impact on modulation schemes and network protocols, on how common they are, and on the consequences for channel modeling. The impact will be different for different schemes and protocols, and how often UWB channels occur remains to be seen. Not all acoustic channels are as strongly wideband as the shown examples.

As far as channel modeling is concerned, it is important that UWB channels violate the WSSUS assumption. UWB channels have correlated taps, even when amplitude and phase fluctuations of the physical paths are uncorrelated. Correlative sounders preserve wideband properties, which are carried by the sidelobes in delay and/or time-varying delays. Hence, direct-replay channel simulation is inherently wideband, whereas simulators based on stochastic replay or physical or statistical modeling face challenges. They have to synthesize the required tap correlation, in one way or another, while simultaneously complying with other requirements such as the correct Doppler spectrum for each tap. The extra effort, modeling complexity, and feasibility depend on the type of model.

REFERENCES

[1] L. Yang and G. B. Giannakis, "Ultra-wideband communications—An idea whose time has come," *IEEE Signal Process. Mag.*, vol. 21, no. 6, pp. 26–54, Nov. 2004.
[2] A. F. Molisch, "Ultra-wide-band propagation channels," *Proc. IEEE*, vol. 97, no. 2, pp. 353–371, Feb. 2009.

[3] R. E. Francois and G. R. Garrison, "Sound absorption based on ocean measurements. Part I: Pure water and magnesium sulfate contributions," *J. Acoust. Soc. Amer.*, vol. 72, no. 3, pp. 896–907, Sep. 1982.

[4] R. E. Francois and G. R. Garrison, "Sound absorption based on ocean measurements. Part II: Boric acid contribution and equation for total absorption," *J. Acoust. Soc. Amer.*, vol. 72, no. 6, pp. 1879–1890, Dec. 1982.

[5] H. Ochi, Y. Watanabe, T. Shimura, and T. Hattori, "Experimental results of short range wideband acoustic communication using QPSK and 8PSK," in *Proc. OCEANS Conf.*, Kobe, Japan, Apr. 2008, DOI: 10.1109/OCEANSKOBE.2008.4531085.

[6] L. Freitag and M. Stojanovic, "Basin-scale acoustic communication: A feasibility study using tomography m-sequences," in *Proc. OCEANS Conf.*, Honolulu, HI, USA, Nov. 2001, pp. 2256–2261.

[7] J. Preisig, "Acoustic propagation considerations for underwater acoustic communications network development," *ACM SIGMOBILE Mobile Comput. Commun. Rev.*, vol. 11, no. 4, pp. 2–10, Oct. 2007.

[8] M. Stojanovic and J. C. Preisig, "Underwater acoustic communication channels: Propagation models and statistical characterization," *IEEE Commun. Mag.*, vol. 47, no. 1, pp. 84–89, Jan. 2009.

[9] P. van Walree, "Channel sounding for acoustic communications: Techniques and shallow-water examples," Forsvarets Forskningsinstitutt, Horten, Norway, FFI-rapport 2011/00007, 2011.

[10] J. M. Jornet, M. Stojanovic, and M. Zorzi, "On joint frequency and power allocation in a cross-layer protocol for underwater acoustic networks," *IEEE J. Ocean. Eng.*, vol. 35, no. 4, pp. 936–947, Oct. 2010.

[11] D. Pompili, T. Melodia, and I. F. Akyildiz, "A CDMA-based medium access control for underwater acoustic sensor networks," *IEEE Trans. Wireless Commun.*, vol. 8, no. 4, pp. 1899–1909, Apr. 2009.

[12] G. L. Turin, F. D. Clapp, T. L. Johnston, S. B. Fine, and D. Lavry, "A statistical model of urban multipath propagation," *IEEE Trans. Veh. Technol.*, vol. VT-21, no. 1, pp. 1–9, Feb. 1972.

[13] J. W. Choi and P. H. Dahl, "Mid- to high-frequency bottom loss in the East China Sea," *IEEE J. Ocean. Eng.*, vol. 29, no. 4, pp. 980–987, Oct. 2004.

[14] E. Y. T. Kuo, "Sea surface scattering and propagation loss: Review, update and new predictions," *IEEE J. Ocean. Eng.*, vol. 13, no. 4, pp. 229–234, Oct. 1988.

[15] A. F. Molisch, "Ultrawideband propagation channels—Theory, measurement, and modeling," *IEEE Trans. Veh. Technol.*, vol. 54, no. 5, pp. 1528–1545, Sep. 2005.

[16] C. R. Berger, W. Chen, S. Zhou, and J. Huang, "A simple and effective noise whitening method for underwater acoustic orthogonal frequency division multiplexing," *J. Acoust. Soc. Amer.*, vol. 127, no. 4, pp. 2358–2367, Apr. 2010.

[17] C. Polprasert, J. A. Ritcey, and M. Stojanovic, "Capacity of OFDM systems over fading underwater acoustic channels," *IEEE J. Ocean. Eng.*, vol. 36, no. 4, pp. 514–524, Oct. 2011.

[18] M. V. Hall, "A comprehensive model of wind-generated bubbles in the ocean and predictions of the effects on sound propagation at frequencies up to 40 kHz," *J. Acoust. Soc. Amer.*, vol. 86, no. 3, pp. 1103–1117, Sep. 1989.

[19] G. B. Deane, "Acoustic screening of the ocean surface by bubbles," in *Proc. Underwater Commun., Channel Model. Validation*, Sestri Levante, Italy, Sep. 12–14, 2012.

[20] P. A. Bello, "Characterization of randomly time-variant linear channels," *IEEE Trans. Commun. Syst.*, vol. 11, no. 4, pp. 360–393, Dec. 1963.

[21] C. R. Berger, S. Zhou, J. C. Preisig, and P. Willet, "Sparse channel estimation for multicarrier underwater acoustic communication: From subspace methods to compressed sensing," *IEEE Trans. Signal Process.*, vol. 58, no. 3, pp. 1708–1721, Mar. 2010.

[22] T. Xu, Z. Tang, G. Leus, and U. Mitra, "Multi-rate block transmissions over wideband multi-scale multi-lag channels," *IEEE Trans. Signal Process.*, vol. 61, no. 4, pp. 964–979, Feb. 15, 2013.

[23] J. C. Preisig and G. B. Deane, "Surface wave focusing and acoustic communications in the surf zone," *J. Acoust. Soc. Amer.*, vol. 116, no. 4, pp. 2067–2080, Oct. 2004.

[24] M. Badiey, A. Song, and K. B. Smith, "Coherent reflection from surface gravity water waves during reciprocal acoustic transmissions," *JASA Exp. Lett.*, vol. 132, no. 4, pp. EL290–EL295, Oct. 2012.

[25] T. C. Yang, "Dispersion and ranging of transient signals in the Arctic Ocean," *J. Acoust. Soc. Amer.*, vol. 76, no. 1, pp. 262–273, Jul. 1984.

[26] D. J. Wingham, "The dispersion of sound in sediment," *J. Acoust. Soc. Amer.*, vol. 78, no. 5, pp. 1757–1760, Nov. 1985.

[27] C. Feuillade, "The attenuation and dispersion of sound in water containing multiply interacting air bubbles," *J. Acoust. Soc. Amer.*, vol. 99, no. 6, pp. 3412–3430, Jun. 1996.

[28] G. Matz, A. F. Molisch, F. Hlawatsch, M. Steinbauer, and I. Gaspard, "On the systematic measurement errors of correlative mobile radio channel sounders," *IEEE Trans. Commun.*, vol. 50, no. 5, pp. 808–821, May 2002.

[29] T. S. Rappaport, *Wireless Communications: Principles and Practice*. Englewood Cliffs, NJ, USA: Prentice-Hall, 1996, pp. 185–186.

[30] P. A. van Walree, T. Jenserud, and M. Smedsrud, "A discrete-time channel simulator driven by measured scattering functions," *IEEE J. Sel. Areas Commun.*, vol. 26, no. 9, pp. 1628–1637, Dec. 2008.

[31] F.-X. Socheleau, C. Laot, and J.-M. Passerieux, "Stochastic replay of non-WSSUS underwater acoustic communication channels recorded at sea," *IEEE Trans. Signal Process.*, vol. 59, no. 10, pp. 4838–4849, Oct. 2011.

[32] J. K. Lewis, J. Rudzinsky, S. Rajan, P. J. Stein, and A. Vandiver, The KauaiEx Group, "Model-oriented ocean tomography using higher frequency, bottom-mounted hydrophones," *J. Acoust. Soc. Amer.*, vol. 117, no. 6, pp. 3539–3554, Jun. 2005.

Paul A. van Walree (M'08) received the M.Sc. and Ph.D. degrees in solid-state physics from Utrecht University, Utrecht, The Netherlands, in 1992 and 1997, respectively.

From 1998 to 2009, he was an Underwater Acoustician at The Netherlands Organisation for Applied Scientific Research (TNO), Delft, The Netherlands. In 2009, he started as a Scientist with the Maritime Systems Department, Norwegian Defence Research Establishment (FFI), Horten, Norway. His research interests include digital underwater communications, channel characterization and simulation, and acoustic signal processing.

Roald Otnes (S'00–M'03) received the M.Sc. and Ph.D. degrees in telecommunications from the Norwegian University of Science and Technology, Trondheim, Norway, in 1998 and 2003, respectively.

Since 2003, he has been a Scientist at the Norwegian Defence Research Establishment (FFI), Horten, Norway. His current research interests include underwater acoustics and signal processing for communications as well as for detection.